

Article

Fusion of Multispectral Remote-Sensing Data through GIS-Based Overlay Method for Revealing Potential Areas of Hydrothermal Mineral Resources

Saad S. Alarifi ^{1,*}, Mohamed Abdelkareem ^{2,*}, Fathy Abdalla ², Ismail S. Abdelsadek ², Hisham Gahlan ¹, Ahmad. M. Al-Saleh ¹ and Mislal Alotaibi ³

¹ Department of Geology and Geophysics, College of Science, King Saud University, P.O. Box 2455, Riyadh 11451, Saudi Arabia

² Geology Department, South Valley University, Qena 83523, Egypt

³ Department of Geosciences, University of Arkansas, Fayetteville, AR 72704, USA

* Correspondence: ssalarifi@ksu.edu.sa (S.S.A.); mohamed.abdelkareem@sci.svu.edu.eg (M.A.)

Abstract: Revealing prospective locations of hydrothermal alteration zones (HAZs) is an important technique for mineral prospecting. In this study, we used multiple criteria inferred from Landsat-8 OLI, Sentinel-2, and ASTER data using a GIS-based weighted overlay multi-criteria decision analysis approach to build a model for the delineating of hydrothermal mineral deposits in the Khnaiguiyah district, Saudi Arabia. The utilized algorithms revealed argillic, phyllic, and propylitic alteration characteristics. The HAZs map resulted in the identification of six zones based on their mineralization potential, providing a basis for potential hydrothermal mineral deposit assessment exploration, which was created by the fusion of mineral bands indicators designated very low, low, moderate, good, very good, and excellent and covers 31.36, 28.22, 20.49, 10.99, 6.35, and 2.59%. Based on their potential for hydrothermal mineral potentiality, the discovered zones match gossans related to sulfide mineral alteration zones, as demonstrated by previous studies.

Keywords: mineral exploration; ASTER; OLI; Sentinel-2; GIS; Khnaiguiyah; Saudi Arabia



Citation: Alarifi, S.S.; Abdelkareem, M.; Abdalla, F.; Abdelsadek, I.S.; Gahlan, H.; Al-Saleh, A.M.; Alotaibi, M. Fusion of Multispectral Remote-Sensing Data through GIS-Based Overlay Method for Revealing Potential Areas of Hydrothermal Mineral Resources. *Minerals* **2022**, *12*, 1577. <https://doi.org/10.3390/min12121577>

Academic Editors: Amin Beiranvand Pour, Omeid Rahmani and Mohammad Parsa

Received: 23 October 2022

Accepted: 6 December 2022

Published: 9 December 2022

Publisher's Note: MDPI stays neutral with regard to jurisdictional claims in published maps and institutional affiliations.



Copyright: © 2022 by the authors. Licensee MDPI, Basel, Switzerland. This article is an open access article distributed under the terms and conditions of the Creative Commons Attribution (CC BY) license (<https://creativecommons.org/licenses/by/4.0/>).

1. Introduction

Remote sensing techniques have provided valuable tools for characterizing and delineating geological, structural, and lithological features that have aided in the identification of mineralization regions [1,2]. Because of its fine geospatial, radiometric, and spectral resolution, remotely sensed data provides significant information for mineral exploration. One of the main aims of remote sensing investigations is the delineation of hydrothermal alteration zones and the identification of the mineralogical signature [1,3,4]. Hydrothermal alteration zones (HAZs) and their grade must be characterized in order to identify possible mineral resource locations [1,2,5,6]. This is due to the fact that such a process is frequently linked to the economic concentration of base metals like Au, Cu, and Ag. Several studies were conducted using multispectral remotely sensed data to characterize the extent of the hydrothermally altered areas and to identify the minerals forming zones [3,7–15].

Data from satellites can be used to detect new prospects prior to detailed and expensive ground research [4,15]. Landsat Operational Land Imager (OLI) and Advanced Spaceborne Thermal Emission and Reflection Radiometer (ASTER) images were used to process and analyze remote sensing multispectral datasets. Electromagnetic (EM) radiation reflected, transmitted, or backscattered from the Earth's surface is sensitive to remote sensing devices such as OLI and ASTER. With passive or active systems, remote sensing sensors can monitor wavelengths of EM radiation in the visible near-infrared and short-wave infrared (VIS/NIR/SWIR) to microwave. Landsat satellite image data have been utilized for lithologic mapping using image transformation techniques [7,8,16–18].

Although Landsat data had been widely used in characterizing hydrothermal alteration zones for decades [8,9,19,20], the introduction of the Advanced Spaceborne Thermal Emission and Reflection Radiometer (ASTER) data in 1999 added meaningful data to the research area of mineral deposits [5,11,12,15,21]. This is due to the fact that, as compared to Landsat data, such data have better spectral, spatial, and radiometric resolutions, allowing for greater information regarding mineral properties.

The capacity of ASTER (e.g., SWIR) spectral bands to distinguish the alteration zones was tested using a variety of methodologies, including band ratios, principal component analysis (PCA), and spectral analysis [5,13,14,21,22]. To improve the spectral disparities across bands and eliminate topographic effects, band ratios were adopted [7,8,13,23]. Mineral indices [11,12,22] and relative absorption band depth (RBD; [24]) were also used. Despite the fact that band ratios, PCA, and RBD have been successful in delineating hydrothermal alteration zones. Many studies have used the band ratios technique to distinguish between different rock units or minerals [4,6].

Because earlier studies did not have such data to use, little emphasis was made on delineating alteration zones and extracting certain important hydrothermal minerals linked with the above-mentioned deposits utilizing remote sensing data in the study area. ASTER spectral bands are thus used in this study to identify the alteration zones associated with Zn-Cu deposits and extract the major hydrothermal alteration zones. This is performed in order to identify prospective mineralization sites in the study area.

Using a GIS-based process to develop mineral development capabilities based on remote data has thus become a rapid and accurate tool for identifying target areas for mineral exploration [4,25], particularly during the reconnaissance stage. Developments in revealing promising areas of hydrothermal mineral resources have been made with the emergence of GIS-based spatial analytic tools [26–29]. This is because employing a GIS method to integrate spatially distributed remote-sensing data is a key approach to mineral exploration since it allows for the combination of different data utilizing digital overlay methods to optimize mineral prospection maps [30]. The GIS-based knowledge-driven technique, for example, is effective in producing predicted maps based on expert opinion [25] since each GIS predictive layer is given a weight that reflects its value in the process.

Prior to the advent of high spectral resolution, multi-spectral sensors, it was challenging to detect alteration zones linked with hydrothermal deposits like those associated with the Khnaiguiyah Zn mineralization. Three sensors' data, e.g., ASTER, Sentinel-2, and OLI spectral bands, are thus used in this study to identify the alteration zones associated with sulfide deposits and extract the major hydrothermal alteration zones. This is performed in order to identify prospective mineralization regions in the Khunayqiyah region.

2. Study Area

The present study is a part of Arabian Shield, Khnaiguiyah, Saudi Arabia. It extends between latitudes $24^{\circ}13'25.48''$ and $24^{\circ}17'43.72''$ and longitudes $45^{\circ}2'47.90''$ and $45^{\circ}6'58.37''$, covering an area of about 57 sq km.

The district of Khnaiguiyah is located at the eastern periphery of the Arabian Shield (Figure 1), which is the exposed Precambrian basement of the Arabian Plate. The Arabian Shield (ANS) is the northernmost extension of the East African Orogen [31,32] and consists of a collage of tectonostratigraphic terranes with ensialic and ensimatic arc affinities [33,34]. The convergence of East and West Gondwana caused the terrane amalgamation/accretion during the Pan-African event (780–600 Ma) [34]. The final suturing (680–610 Ma) of the ANS coincided with the development of the Nabitah fault zone, gneiss domes, and massive Molasse basins [35,36]. The NW–SE trending Najd fault system/Najd Orogeny (620–540 Ma) subsequently formed due to escape tectonics concomitant with the assembly of the Gondwana supercontinent [37,38]. By the Cambrian (541 Ma), the ANS was established as a stable juvenile continental block forming the northeastern margin of Gondwana [39].

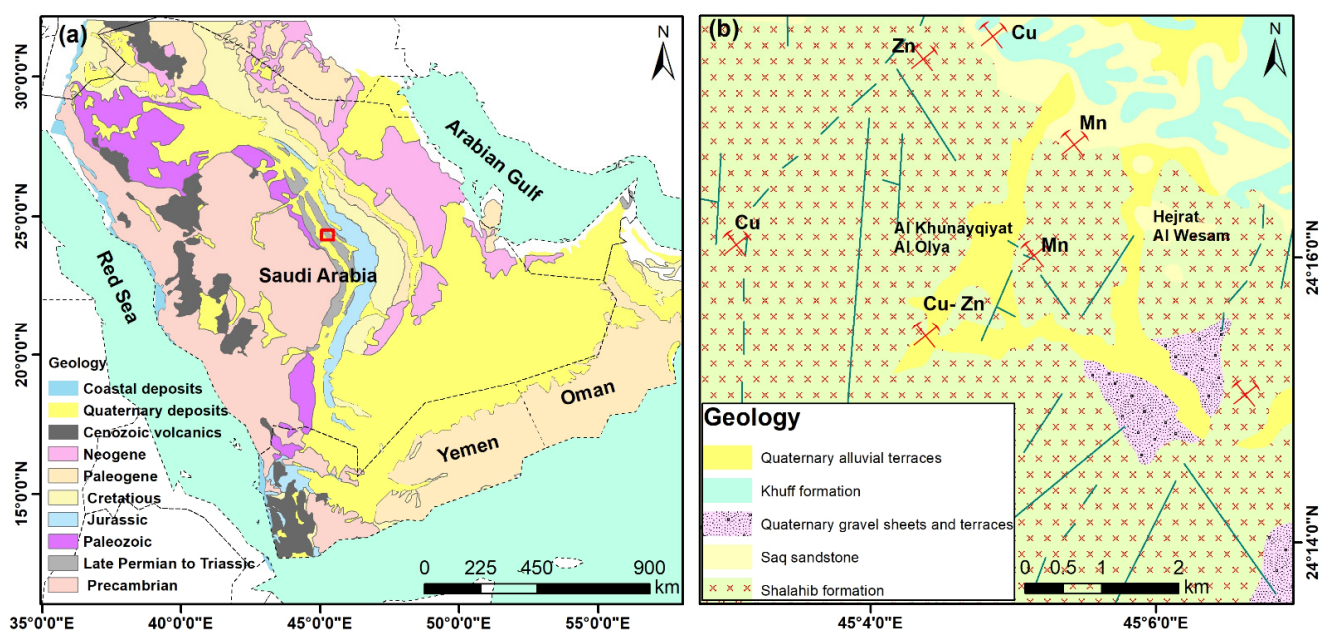


Figure 1. (a) General geologic map of the Arabian Peninsula showing the location of the Khnaiguiyah mineralized district; (b) simplified geologic map of the Khnaiguiyah area denoting the main mineral occurrences.

Khnaiguiyah Zn–Cu deposits represent a substantial zinc resource and attracted considerable exploration efforts in the last three decades [40]. The four ore bodies of the Khnaiguiyah district comprise mineable reserves of up to 11 Mt averaging 7.41% Zn and 0.82% Cu [41]. Khnaiguiyah-type deposit features are consistent with metamorphism and deformation of volcanogenic massive sulfide (VMS) mineralization; the related stratiform Mn-rich units are mainly suggestive of a seafloor hydrothermal setting.

The Khnaiguiyah ores are hosted by the Shalahib Formation (1500 m thick), which is made up of felsic volcano-sedimentary rocks interlayered with carbonates [42]. The Shalahib formation predominantly comprises andesite and rhyolite volcanic rocks and associated pyroclastics and ignimbrites, and the whole sequence is affected by low-temperature greenschist-facies regional metamorphism. The Khnaiguiyah deposit lies within an area of 3×3 km. Four mineralized orebodies are interpreted hydrothermal mineral deposits containing Zinc and Copper that are hosted by strongly sheared and folded late Proterozoic medium to felsic volcanics/volcaniclastics. The shear zones, which are tens of meters thick, are oriented NS and dip 10 to 70 to the west. The hydrothermally altered rocks occur within discontinuous anastomosed bands 50 to 100 m wide and several Kilometers long and are regionally oriented along with the north–south regional foliation. Detailed analysis of surface and drill-core samples shows that the hydrothermal alteration zones and associated Zn–Cu–Fe–Mn mineralization are controlled by a shearing deformation phase that post-dated the first phase of regional folding. The hydrothermal alteration zone contains illite, kaolinite, quartz, albite, hematite, and calcite.

At this locality, the Precambrian basement is overlain by the basal conglomerates and cross-bedded red sandstone of the middle Cambrian Saq formation, which is in turn overlain by the Permo-Triassic shallow marine carbonates of the Khuff formation.

3. Data Used and Methods

This study used visible/infrared satellite-derived imagery to characterize mineralization associated with hydrothermal alteration zones. Landsat 8-OLI, Sentinel-2, and ASTER data (Figure 2) were all employed to detect altered features and structural patterns. A comparison of these sensors is shown in Figure 2 [19].

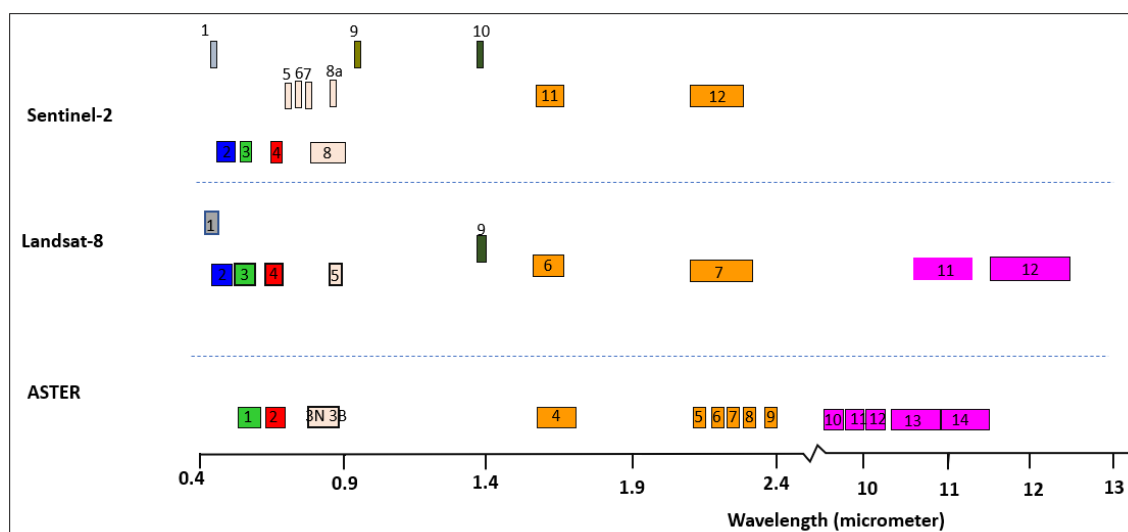


Figure 2. Comparison between ASTER, Landsat 8, and Sentinel-2.

On 11 February 2013, the Landsat-8 (OLI) satellite was launched. Landsat-8 scene dimension is 85-km-cross-track-by-180-km-along-track. There are nine VIS/NIR and SWIR ranges reported, as well as two longwave thermal ranges. The pixel size of OLI channels was stated to be 30 m; however, TIRS has a spatial resolution of 100 m. The quantization level is 12-bit data that permits additional bits to be used to acquire optimal data, enabling the assessment of minor surface disturbances. Landsat-OLI scene (path/row 166/43; ID: LC08_L1TP_166043_20211209_20211215_01_T1) that was acquired on 9 December 2021.

NASA and METI (Japan's Ministry of Economic Trade and Industry) deployed ASTER, an advanced multispectral satellite imaging system, onboard the TERRA spacecraft in December 1999. NASA's Land Processes Distributed Active Archive Centre provided the ASTER data (LP DAAC). ASTER data includes spectral ranges in the visible and near-infrared (VNIR), shortwave infrared (SWIR), and thermal infrared (TIR): three bands (with 15 m spatial resolution) in the VNIR, six bands (with 30 m spatial resolution) in the SWIR, and five bands (with 90 m spatial resolution) in the TIR (TIR). In this investigation, the ASTER SWIR spectral bands (30 m spatial resolution) are used to measure between ~ 1.60 and $2.45 \mu\text{m}$ to allow discriminating between Al-OH, Fe, Mg-OH, H-O-H, and CO_3 absorption features [43].

Preprocessing of the obtained ASTER scene (ASTER data ID: ASTB061106074035) included cross-talk correction and data orthorectification using the ENVI software application. Using ENVI v.5 software, the Log-residual (LR) technique was used to calibrate, normalize, and decrease noise from sensors and solar illumination in SWIR bands [2,14]. On ASTER data, this approach was used to remove atmospheric and topography impacts. As a result, the data became more reflective of the target area's composition and lithology. It was also possible to compare the retrieved endmembers of SWIR bands to reference spectra from the spectral library of the United States Geological Survey (USGS). This approach was used to reveal minerals using SWIR data [14,44].

On 23 June 2015, the Sentinel-2A satellite was launched, and the first data was taken a few days later. Sentinel-2 sensors gather data in the VIS/NIR, and SWIR, TIR wavelength ranges. These bands have a spatial resolution of 10–60 m. Sentinel-2 captures 13 bands in the VIS/NIR and SWIR spectrum. The VIS/NIR bands: blue B2 (490 nm), green B3 (560 nm), red B4 (665 nm), and infrared B8 (842 nm) have a 10 m pixel size, whilst the coastal band B1 (443 nm) has a 60 m pixel geometry. The pixel sizes of the SWIR bands (B11: 1610 nm, B12: 2190 nm) are both 20 m. Sentinel-2 scene (S2A_MSIL1C_20211221T073331_N0301_R049_T38QNM_20211221T084355) is delivered as zip-compressed files in Sentinel's own SAFE format. The spectral bands are stored as jpg files in this SAFE file in three different geometric resolutions (10 m, 20 m, and 60 m). The

jpg files of bands B2, B3, B4, and B8 with a spatial resolution of 10 m, and B11 and B12 with 20 m are stacked into a single GeoTIFF file of a uniform pixel size of 10 m. A subset of these data was conducted during preprocessing using SNAP software in order to minimize the computational time and the data.

To analyze multispectral data, several methods have been used, including PCA, the utilization of band ratios, relative absorption band depth (RBD; 24), and mineral indices [11,12,22], as well as spectral analysis. Band ratios have been employed to investigate spectral differences between bands and to reduce topographic impacts [7,8,23,45]. The intensity of the hydrothermal activity can be used to reveal hydrothermal mineral assemblages [13,28]. Sub-pixel spectral classifications can thus be attributed to specific important hydrothermal minerals associated with propylitic (epidote, chlorite, calcite), phyllic (muscovite, sericite, illite), argillic (montmorillonite, kaolinite, dickite), and advanced argillic (alunite–pyrophyllite) alteration zones.

The band ratio is a transformation procedure for enhancing spectral differences in remote sensing data. It works by dividing pixels from one band by pixels from another band [46] and sometimes dividing bands of the numerator or/and denominator after mathematical calculation. The goal of this technique is to reveal the spectral characteristics of material so that variables on Earth’s surface can be distinguished better [47]. Band ratios can be used to distinguish between soils, rock types, and land use effects [48–51]. The ENVI software and ArcGIS software packages v. 10.8 are utilized in the present study. The PCA process has been used to transform a large number of correlated spectral bands into a smaller number of uncorrelated spectral bands, which is a statistical approach used in image transformation. In the mapping of hydrothermal potential alteration zones, the selective “principal components” (PCs) technique has been frequently used [5,15]. Based on the eigenvectors of the selected bands, statistical parameters were examined to determine which PC image could be utilized to emphasize the particular minerals.

Spectral mapping was used to differentiate mixed pixels from unwanted pixels during the mineral extraction process. This enabled the mapping and identification of possible minerals based on the end member’s spectral signature in comparison to those in the spectral library [5,14]. The MNF transformation [52] was used to derive a PPI that represented the input image’s most spectrally pure pixels. This was utilized to detect endmembers using n-D visualization for mineral identifications based on spectral classifications. Using MNF and PPI, the n-D visualize viewer can locate, characterize, cluster (group), and pick the purest pixels (endmembers) in n-spaces. Each class indicated a mineral with a high absorption capacity.

Digital overlay approaches have been utilized to create integrative maps using Geographic Information System (GIS) technologies [28,29,53]. Predictive maps have also been created using knowledge-driven systems using weighted overlay analysis of ArcGIS that integrate multi-criteria decision-making based on expert judgment [30,54]. Each evidential image was reclassified into five classes using the Natural Breaks method; the class of high intensity of hydrothermal alteration is given “5” and the opposite given “1. As a result, the final prospective map can be created by combining several evidential maps [54].

4. Results

4.1. Lithologic and Structural Characteristics

Goethite, hematite, and jarosite are examples of iron minerals that have diagnostic spectral characteristics near 0.43 m, 0.65 m, 0.85 m, and 0.93 m, which are close to Sentinel-2 band 1, band 4, band 8/8A, and band 9 [55]. Moreover, both hematite and jarosite exhibit reflectance characteristics near 0.72 m and 0.74 m, which are both close to Sentinel-2 band 6. Hematite also displays a distinguishing absorbance pattern at a wavelength of 0.88 m, which corresponds to Sentinel-2A band 8A. Thus, Sentinel-2 band ratios of 6/1, 6/8A, and (6 + 7)/8A were utilized to distinguish hematite + goethite, hematite + jarosite, and a mixture of iron-bearing minerals (see more information on iron mineral spectra in Ge et al. [55]) from felsic or sedimentary deposits in red from basement mafic to intermediate

variations in cyan (See Figure 3a) as they contain ferromagnesian minerals [2]. Sentinel-2 (Figure 3b) uses 11/8A, 3/4, and (6 + 7)/8A of ferric, ferrous, and a combination of iron-containing minerals to indicate likely areas rich in hydrothermal alteration in purple, mafic varieties in yellow, and sedimentary deposits in the northeast in red-orange, but vegetation in green. Images from the Sentinel-2 satellite (Figure 3c) 11/12, 11/8A, and (6 + 7)/8A displayed white-toned patches in HAZs [2]. The study's heights (Figure 3d) vary from 789 to 933 m above sea level, and the majority of the structural patterns are visible at these elevations.

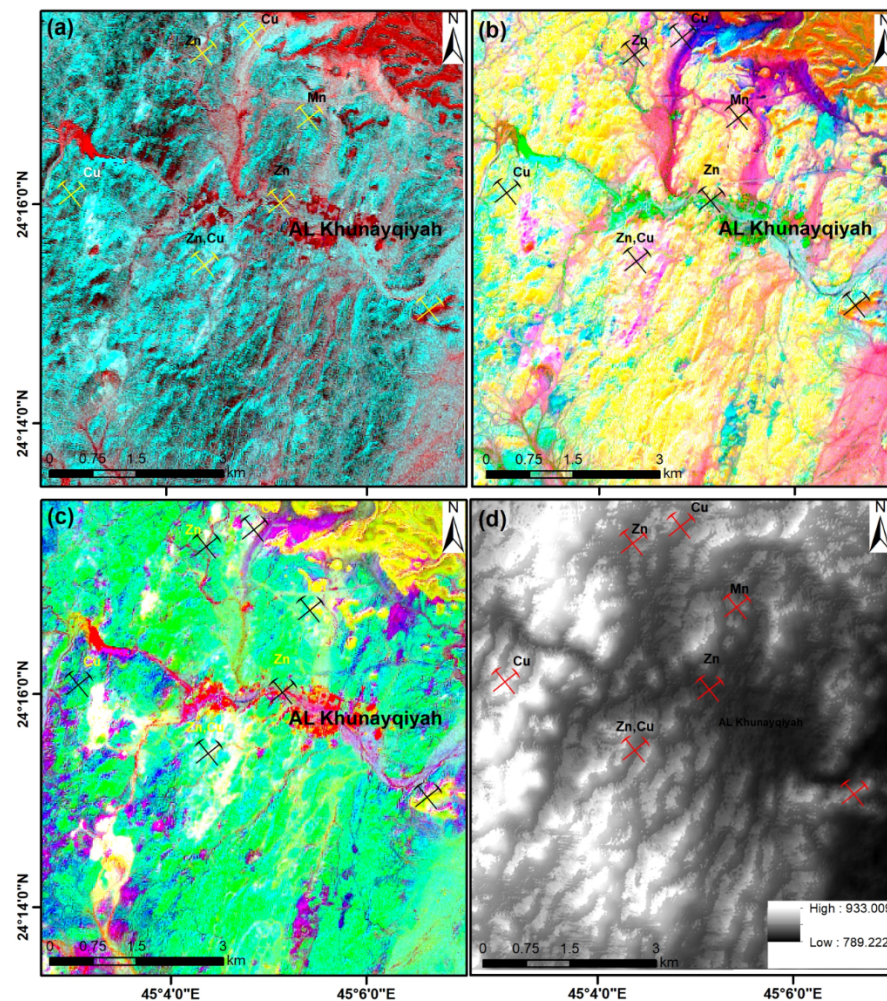


Figure 3. (a) band ratio 6/1, 6/8A, and (6 + 7)/8A; (b) 11/8A, 3/4, and (6 + 7)/8A; (c) 11/12, 11/8A, and (6 + 7)/8A; (d) DEM derived from Geo-Eye data.

4.2. Hydrothermal Alteration Zones

4.2.1. Landsat-8

Band ratios are used to enhance hydrothermally altered zones and the oxidation zone that reflects the abundance of certain minerals. Band ratios 6/7, 6/2, and $6/5 * 4/5$ [16] were employed to improve the identification of rocks and minerals based on content mineralogy (Figure 4a,b). Band ratio 6/7 is susceptible to OH-bearing minerals, and band ratio 6/2 highlights rocks rich in FeO composition, so mafic igneous rocks have lower reflectance than other igneous rocks; and band $6/5 * 4/5$ is useful to distinguish between mafic and non-mafic rocks based on their sensitivity to high Fe-bearing aluminosilicate concentration. Iron-bearing minerals and OH-bearing minerals are abundant in these areas. Sultan et al. [16] demonstrated that rationing in the $6/5 * 4/5$ band is possible. Sultan et al. [16] use the sensitivity of the ratio to Fe-bearing aluminosilicates to distinguish mafic

rocks (bluish color) from other rocks. Ramadan et al. [56] revealed the potential locations of hydrothermal mineral deposits in 6/7, 6/5, and 5 (Figure 4c,d). Using the band ratios 6/7, 4/2, and 5/6 in R, G, and B [7], felsic rocks are colored green, mafic rocks are colored blue, and areas of extensive hydrothermal alteration are colored light pink, yellow, and light red (Figure 4a,c,e, respectively). The 6/7 ratio emphasizes hydrothermal alteration and surface weathering oxides and hydroxides [23,57,58]. Clay minerals have a high Band 6 reflectance and a strong Band 7 absorption [10,58]. The 4/2 ratio is important for detecting iron oxide-bearing rocks (Figure 4e) due to considerable absorption in Band 2 and reflectance characteristics in Band 4 for iron oxides [7]. The felsic rocks in 4/2 appear in green color.

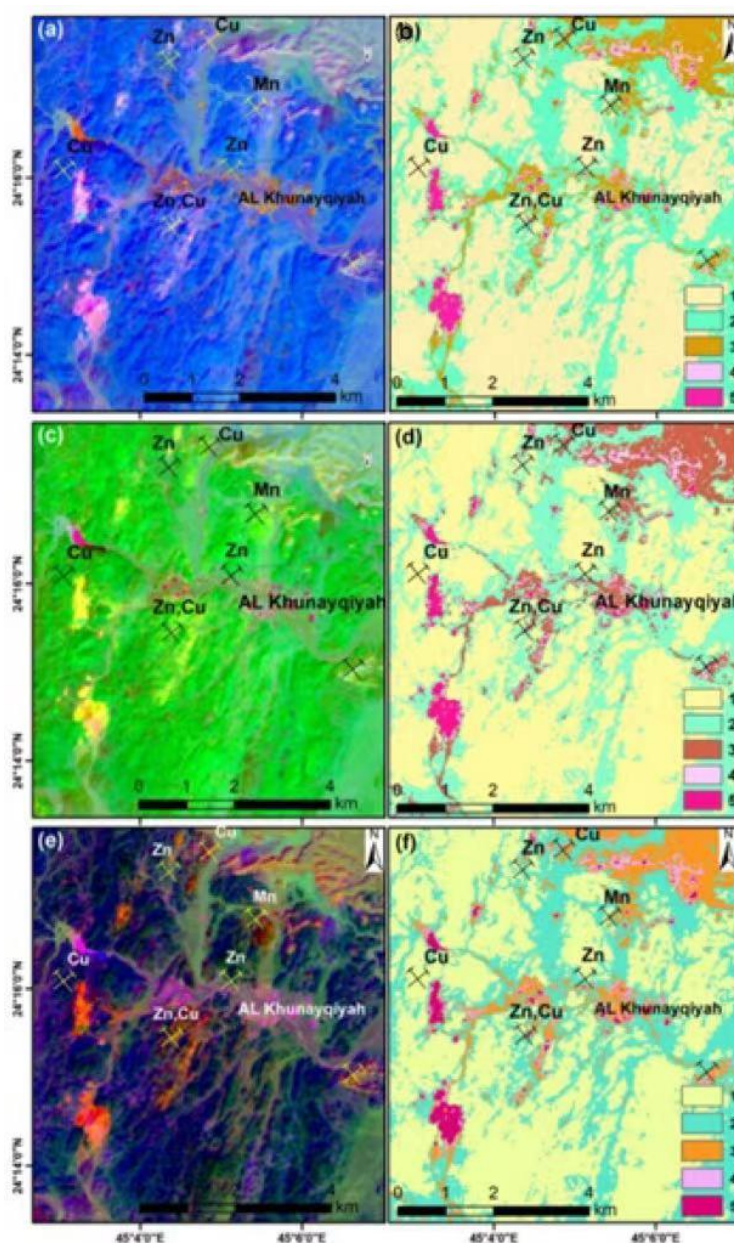


Figure 4. (a) Band ratios 6/7, 6/2, and 6/5 * 4/5, (b) reclassify of 6/7, 6/2, and 6/5 * 4/5, (c) 6/7, 6/5, 5 of Ramadan; (d) reclassify of 6/7, 6/5, 5; (e) Band ratios composite (6/7, 4/2, 5/6) Abrams; (f) reclassify of (6/7, 4/2, 5/6).

4.2.2. Sentinel-2

As shown in (Figure 5a), [59] offered three band ratios in R, G, and B: 11/12, 11/8, and 4/2. These band ratios were utilized in this research to distinguish the alteration zones. These ratios are proportional to the occurrence of OH-bearing minerals (11/12), iron oxides (4/2), and the band ratio 6/5, which is utilized to enhance the presence of ferrous oxides. Metavolcanics are colored green in this ratio, indicating high ferrous oxide content. Some wadi deposits have a purple tint due to the occurrence of clay minerals and iron-bearing minerals in high concentrations. The locations of probable HAZs are revealed in a yellow color due to their high presence of clay and ferrous oxides.

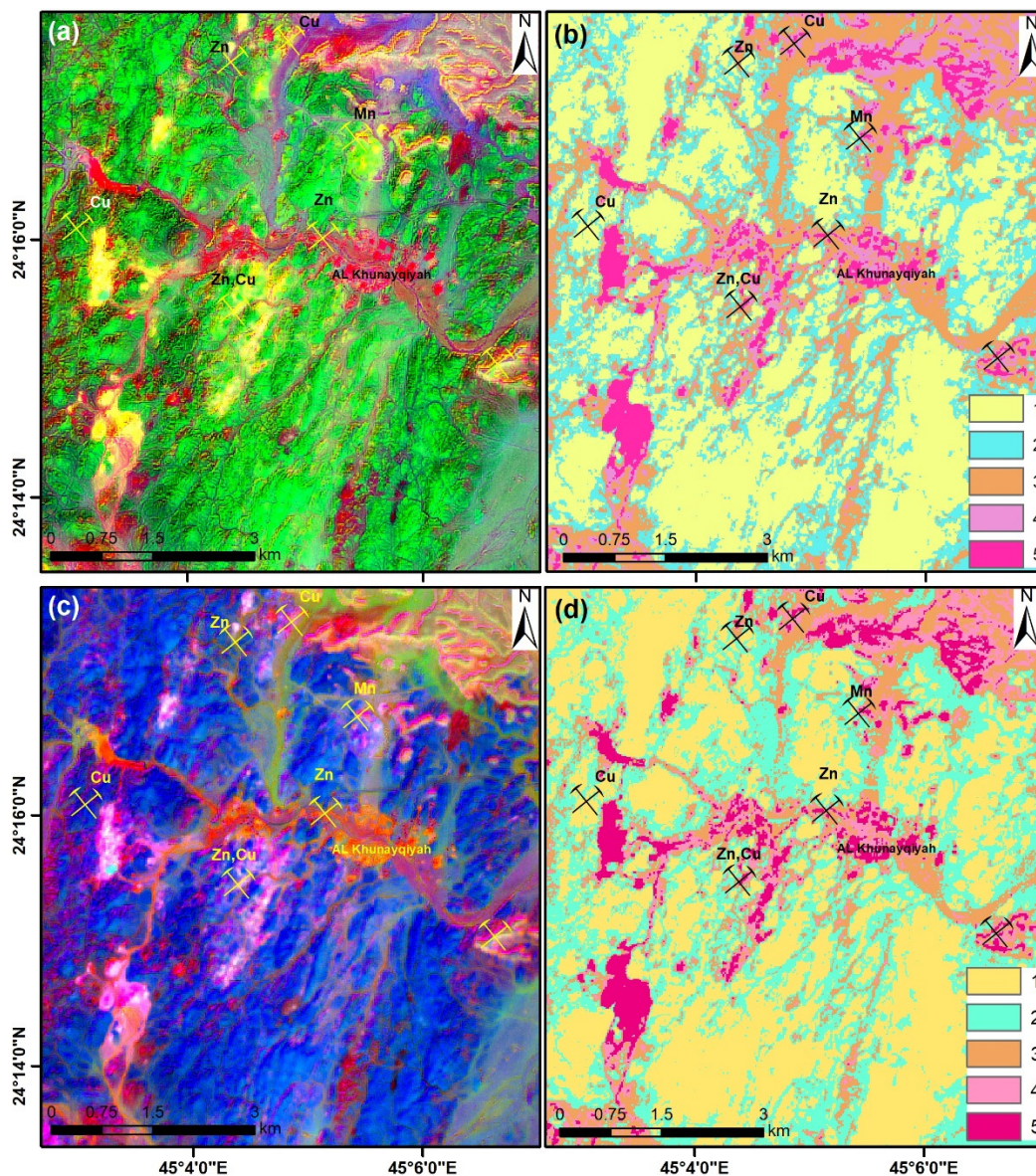


Figure 5. Sentinel-2 (a) Band ratios 11/12, 11/8, and 4/2; (b) reclassify of 11/12, 11/8, and 4/2; (c) 11/12, 11/2, and 11/8 * 4/8; (d) reclassify of 11/12, 11/2, and 11/8 * 4/8.

To improve the identification of rock units based on mineral content, ratio bands of 11/12, 11/2, and 11/8 * 4/8 [16] were used (Figure 5b,c). Band ratio 11/12 is amenable to OH-bearing minerals; band ratio 11/2 is associated with the content of opaque minerals (e.g., FeO) in rocks, so mafic rock types have lesser reflectance than some other igneous rocks; and band 11/8 * 4/8 can be used to distinguish between mafic and non-mafic rocks

based on their sensitivity to high Fe-bearing aluminosilicate concentration. Iron-bearing minerals and OH-bearing minerals are widespread in such regions.

4.2.3. ASTER

The OH-bearing minerals have reflectance at 1.656 μm (band 4). The argillic minerals (montmorillonite and kaolinite) contain absorption features at 2.205 (band 6), and kaolinite display double-shaped absorption features around 2.165 (band 5) and 2.205 (band 6), in contrast to phyllic minerals (muscovite and illite), which have a single deep absorption feature at 2.205 (band 6) (Figure 6; from Mars and Rowan [3]). Propylitic minerals with a 2.335 μm absorption characteristic. This most likely matches minerals like calcite and chlorite that contain CaCO_3 or Mg-OH [3].

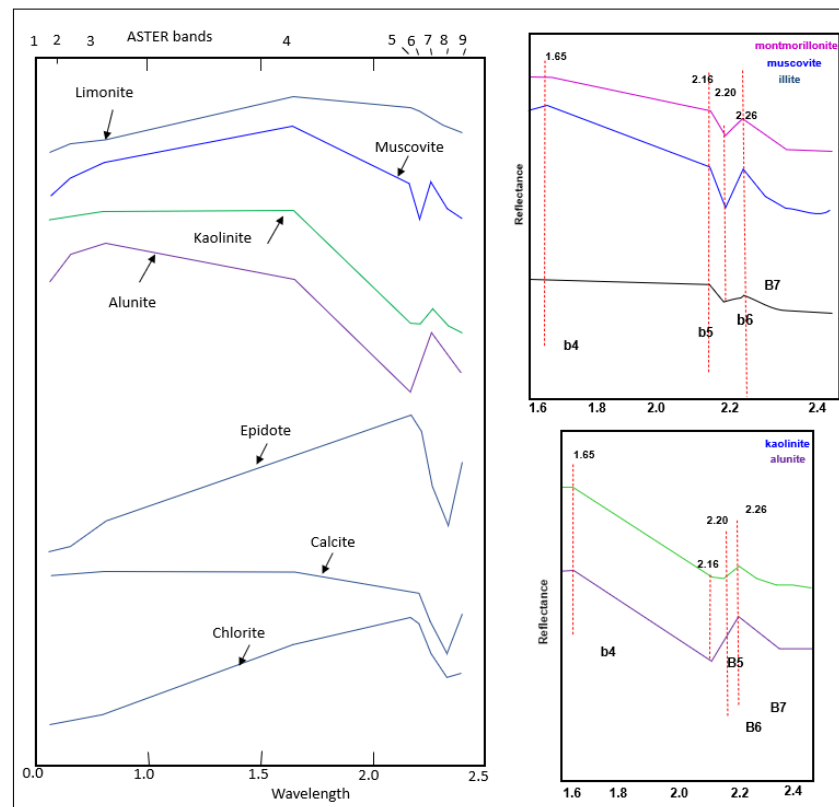


Figure 6. Mineral spectra of minerals and ASTER bands.

The ASTER band ratios 4/6, 4/5, and 4/7 boost argillic and sericitic alteration zones, respectively [6]. Furthermore, in these images, the ASTER– 4/5 band ratio defines the advanced argillic alteration (e.g., alunite and dickite). As a result, the combination of band ratios 4/6, 4/5, and 4/7 in R, G, and B of ASTER is utilized to depict HAZs. Figure 7 depicts the classification of these combined ratios into five ranks of hydrothermal alteration, with the highest rank (0.60–0.64) in red, denoting locations with both argillic and sericitic regions of alteration.

Figure 7c,d shows the results of merging band ratio images 4/6, 7/6, and $(5 + 7)/6$. Regions richer in white mica were identified using the band ratio of 7/6. Using such ratios, locations rich in Al-OH minerals are depicted in a white tone. The largest band ratios of 4/6 and 7/6 refer to the phyllic zone [60], and the values of $(5 + 7)/6$ are also true. The green-colored area has less hydrothermal alteration than the first, but pink-colored portions have the least amount of HAZs. Band ratios 4/6 in this composite highlight the white tone's alteration zones (Figure 7). Furthermore, band ratios of 7/6 were applied to determine the areas of an abundance of Al-OH minerals as white mica (muscovite) as revealed in white tone, which occupies the middle part of the present study area (Figure 7).

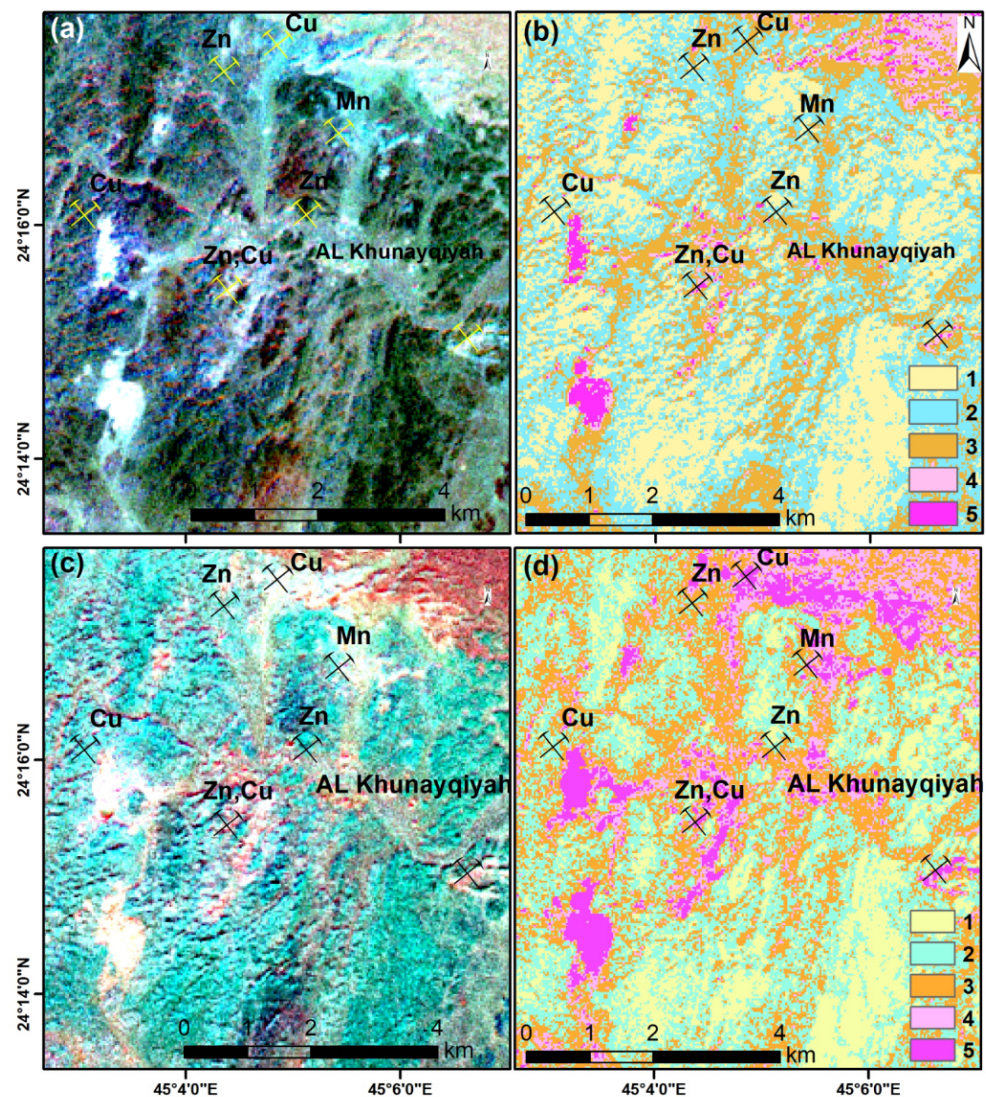


Figure 7. ASTER (a) band ratios 4/6, 4/5, and 4/7; (b) reclassify band ratios 4/6, 4/5, and 4/7; (c) 4/6, 7/6, and (5 + 7)/6; (d) reclassify 4/6, 7/6, and (5 + 7)/6.

The contrast between hydrothermally altered zones was emphasized by the combination of band ratios $(5 + 7)/6$, $(4 + 6)/5$, and $(7 + 9)/8$ in R, G, and B, respectively (Figure 8a). This allowed areas richer in phyllic, argillic [6,61], and propylitic minerals to be detected, respectively. In this combination, yellow areas revealed argillic and phyllic hydrothermal alterations. PCA was used to map areas of argillic hydrothermal alteration using ASTER bands 4, 5, and 6b. Table 1 shows the eigenvector values obtained using the specific bands (B4, B5, and B6) for the PCA method (Table 1). PC2 indicates a negative loading of band 4 (-0.780) and a positive loading of bands 5 (0.605) and 6 ($= 0.157$) according to eigenvector loadings. The locations of hydrothermal alteration are revealed in a white tone when negated (multiplied by -1) PC2 is displayed in greyscale (Figure 8b).

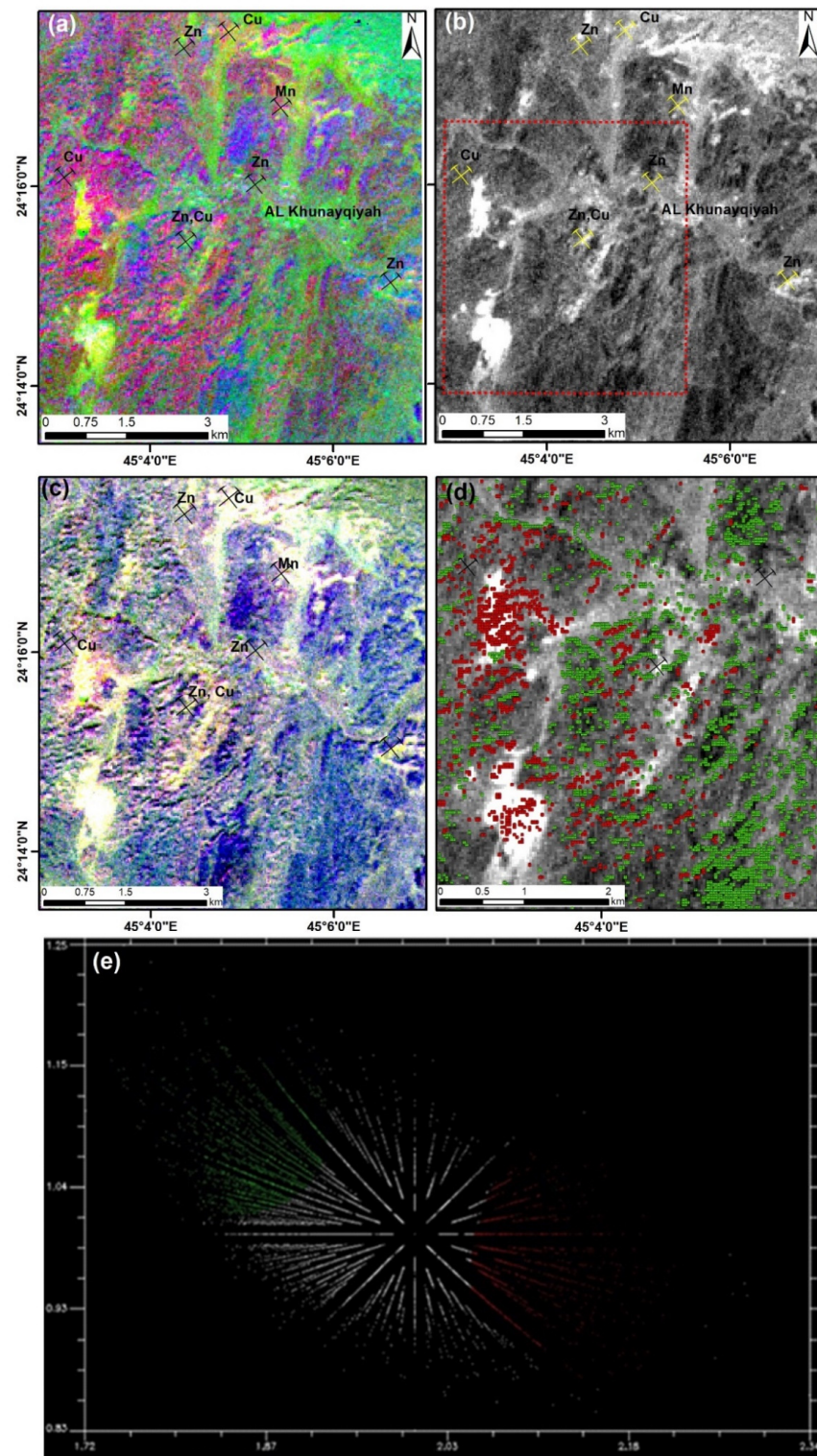


Figure 8. ASTER (a) band ratios composite (5 + 7)/6, (4 + 6)/5, and (7 + 9)/8 in R, G, and B; (b) OHI, KAI, and ALI in R, G, and B; (c) Negated PC2 of selected bands 4, 5, and 6; (d) subset of “c” image overlain by extracted interest pixels of Scattergram of the ASTER derived bands 5 + 7/6 ‘Al-OH content’ vs. bands 5/7 (outside absorption) ‘Al-OH composition’ (Cudahy et al. 2008) in “(e)”. The AL-OH area rich in minerals marked in red are consistent with the areas of high hydrothermal alteration.

Table 1. PCA of selected bands 4, 5, and 6.

Eigenvector	Band 4	Band 5	Band 6	Eigenvalue
PC1	−0.5646	−0.57235	−0.59468	99.923
PC2	−0.7798	0.605985	0.157136	0.057
PC3	−0.27043	−0.55245	0.788457	0.021

The band ratios OHI, KAI, and ALI were integrated into R, G, and B to distinguish between potential sites of argillic and phyllic alteration. The areas of increased hydrothermal alteration are congruent with structural features associated with granitic rocks, according to the classifications of these combined values. Each fraction's greatest value is denoted by a white tone. The minerals indices OHI, KLI, and ALI were displayed in R, G, and B, respectively (Figure 8c), and locations with abundances of the three indices of OHI, KAI, and ALI are emphasized in white tone.

OHI bearing altered minerals Index (OHI) = [band 7/band 6] × [band 4/band 6]

Kaolinite Index (KLI) = [band 4/band 5] × [band 8/band 6],

Alunite Index (ALI) = [band 7/band 5] × [band 7/band 8]

A subset image of PC2 (Figure 6d) is overlain by extracted interest pixels derived from the scattergram (Figure 6e). A two-dimensional (2D) scatter plot of band ratios (5 + 7)/6 (Al-OH content) vs. 5/7 (Al-OH composition) was used to explore ASTER Al-OH composition [62]. The diagram's extreme far bottom right side indicated regions with no Al-OH minerals, whereas the extreme top left side of the diagram revealed places with no Al-OH minerals. Cudahy et al. [62] found that plotting band ratios (5 + 7)/6 (Al-OH content) vs. 5/7 (Al-OH composition) clearly separated areas rich in Al-OH from those with no Al-OH, confirming prior findings. Higher values, indicating higher Al-OH concentrations, are highlighted in red and correspond to locations of significant hydrothermal alteration. As illustrated by the green in Figure 8e, this area was clearly delimited by lower Al-OH concentration and higher Mg-OH content.

5. XRD Analysis of Hydrothermal Alteration Zones

Samples were taken from the two main alteration zones (Figure 9), and 21 representative specimens were selected for XRD analysis at the National Research Center (Egypt). The results of the analyses revealed the presence of silica minerals (mostly quartz), gypsum, anhydrite, kaolinite, illite, clinocllore, and hematite, with a small percentage of microcline, calcite, and halite (Tables 2 and 3). Clay minerals (kaolinite, illite, sericite) in these zones are mainly the products of the decomposition of plagioclase feldspar, and the presence of ferric iron oxides and hydroxides (hematite, goethite) is related to the weathering of ferromagnesian minerals (mostly hornblende and clinopyroxene). The abundance of sulfates in the form of gypsum and anhydrite is highly indicative of the former presence of disseminated sulfide phases, which is compatible with these zones being either mature gossans or conduits within the feeder zones beneath massive sulfide mounds.

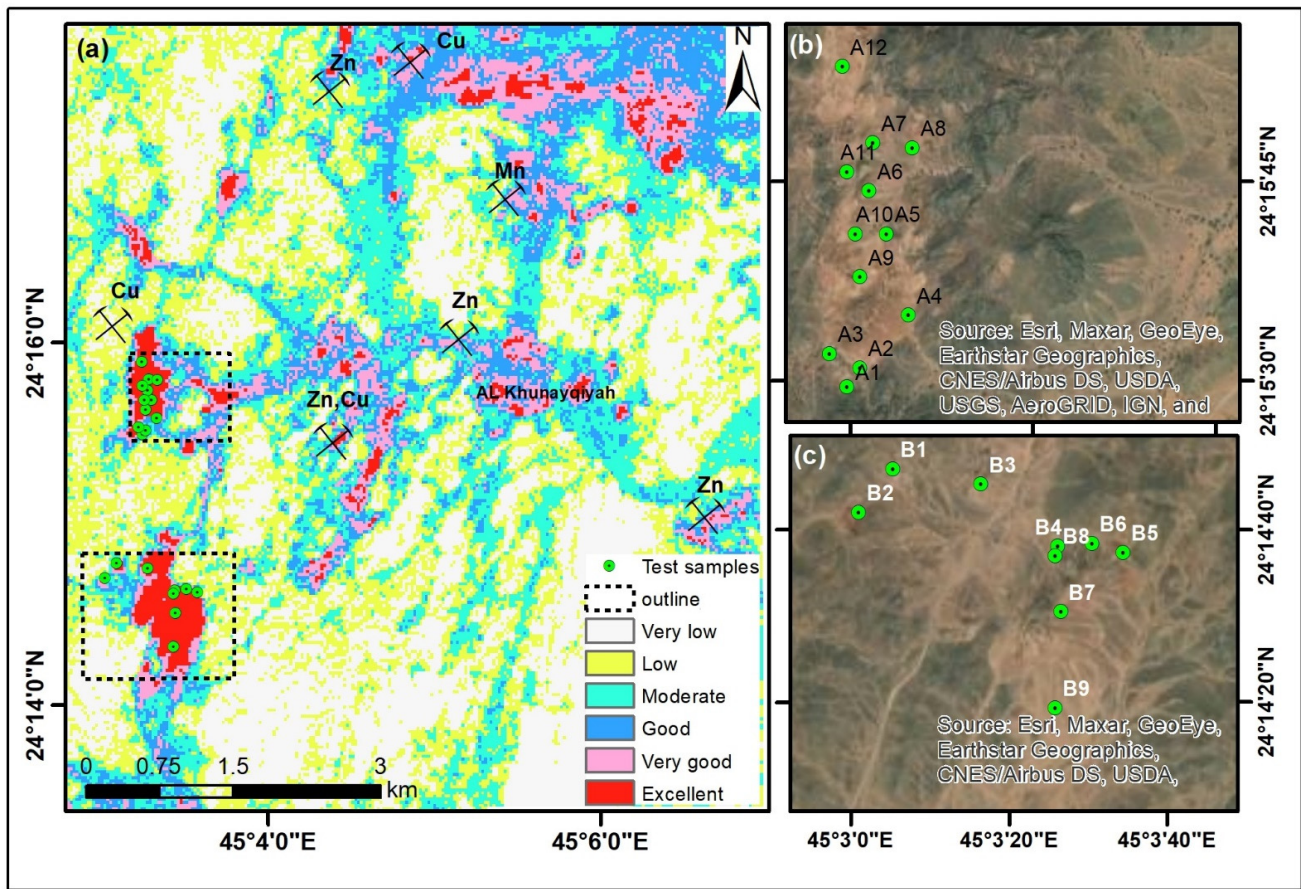


Figure 9. (a) Mineral perspective map of the study area; (b,c) Maps show sample locations that were selected for XRD analysis. A shows sample location for Table 2. B shows the samples location for Table 3.

Table 2. The results of XRD analysis; see Figure 9b for the location map.

Sample Name	Compound Name	Chemical Formula	Vol %
A1	Quartz	SiO ₂	25.8
	Gypsum	CaSO ₄ ·2H ₂ O	61.9
	Illite	K _{0.5} (Al,Fe,Mg)3Si ₃ AlO ₁₀ (OH) ₂	9.7
	Anhydrite	CaSO ₄	2.6
A2	Quartz	SiO ₂	5.7
	Gypsum	CaSO ₄ ·2H ₂ O	90.2
	Kaolinite	Al ₂ Si ₂ O ₅ (OH) ₄ /Al ₂ O ₃ ·2SiO ₂ ·2H ₂ O	3.0
	Anhydrite	CaSO ₄	7.1
A3	Quartz	SiO ₂	43.1
	Kaolinite	Al ₂ Si ₂ O ₅ (OH) ₄ /Al ₂ O ₃ ·2SiO ₂ ·2H ₂ O	18.9
	Illite	KAl ₂ Si ₃ AlO ₁₀ (OH) ₂	31.5
	Anhydrite	CaSO ₄	6.6
A4	Quartz	SiO ₂	62.50
	Gypsum	CaSO ₄ ·2H ₂ O	12.30
	Illite	KAl ₂ Si ₃ AlO ₁₀ (OH) ₂	18.8
	Hematite	Fe ₂ O ₃	6.4

Table 2. Cont.

Sample Name	Compound Name	Chemical Formula	Vol %
A5	Quartz	SiO ₂	41.5
	Gypsum	CaSO ₄ ·2H ₂ O	24.9
	Illite	KAl ₂ Si ₃ AlO ₁₀ (OH) ₂	3.1
	Kaolinite	Al ₂ Si ₂ O ₅ (OH) ₄ /Al ₂ O ₃ ·2SiO ₂ ·2H ₂ O	17.1
	Hematite	Fe ₂ O ₃	2.0
	Clinocllore	Mg ₅ Fe ₀ ·2Al ₂ Si ₃ O ₁₀ (OH) ₈	11.3
A6	Quartz	SiO ₂	62.8
	Hematite	Fe ₂ O ₃	3.1
	Illite	KAl ₂ Si ₃ AlO ₁₀ (OH) ₂	24.5
	Anhydrite	CaSO ₄	9.6
A7	Quartz	SiO ₂	47.2
	Gypsum	CaSO ₄ ·2H ₂ O	21.2
	Illite	KAl ₂ Si ₃ AlO ₁₀ (OH) ₂	10.6
	Halite	NaCl	3.2
	Bassanite	CaSO ₄ ·0.5H ₂ O	17.7
A8	Quartz	SiO ₂	20.0
	Gypsum	CaSO ₄ ·2H ₂ O	72.5
	Illite	KAl ₂ Si ₃ AlO ₁₀ (OH) ₂	7.6
A9	Quartz	SiO ₂	70.8
	Gypsum	CaSO ₄ ·2H ₂ O	21.2
	Calcite	CaCO ₃	8.0
A10	Quartz	SiO ₂	38.3
	Gypsum	CaSO ₄ ·2H ₂ O	35.8
	Illite	KAl ₂ Si ₃ AlO ₁₀ (OH) ₂	20.1
	Anhydrite	CaSO ₄	5.9
A11	Quartz	SiO ₂	48.4
	Gypsum	CaSO ₄ ·2H ₂ O	18.1
	Illite	KAl ₂ Si ₃ AlO ₁₀ (OH) ₂	15.9
	Anhydrite	CaSO ₄	4.9
	Hematite	Fe ₂ O ₃	4.1
	Kaolinite	Al ₂ Si ₂ O ₅ (OH) ₄ /Al ₂ O ₃ ·2SiO ₂ ·2H ₂ O	8.6
A12	Quartz	SiO ₂	57.3
	Albite	NaAlSi ₃ O ₈	10.2
	Illite	KAl ₂ Si ₃ AlO ₁₀ (OH) ₂	6.4
	Microcline	KAlSi ₃ O ₈	13.6
	Calcite	CaCO ₃	12.4

Table 3. The results of XRD analysis; see Figure 8b for the location map.

Sample Name	Compound Name	Chemical Formula	vol %
B1	Quartz	SiO ₂	37.5
	Gypsum	CaSO ₄ ·2H ₂ O	28.1
	Kaolinite	Al ₂ Si ₂ O ₅ (OH) ₄ /Al ₂ O ₃ ·2SiO ₂ ·2H ₂ O	28.1
	Illite	KAl ₂ Si ₃ AlO ₁₀ (OH) ₂	3.4
	Bassanite	CaSO ₄ ·0.5H ₂ O	2.8
B2	Quartz	SiO ₂	11.4
	Gypsum	CaSO ₄ ·2H ₂ O	73.0
	Albite	NaAlSi ₃ O ₈	8.7
	Calcite	CaCO ₃	7.0

Table 3. Cont.

Sample Name	Compound Name	Chemical Formula	vol %
B3	Quartz	SiO ₂	65.3
	Kaolinite	Al ₂ Si ₂ O ₅ (OH) ₄ /Al ₂ O ₃ ·2SiO ₂ ·2H ₂ O	9.8
	Calcite	CaCO ₃	8.2
	Hematite	Fe ₂ O ₃	0.8
	Microcline	KAlSi ₃ O ₈	15.9
B4	Quartz	SiO ₂	4.3
	Gypsum	CaSO ₄ ·2H ₂ O	91.8
	Kaolinite	Al ₂ Si ₂ O ₅ (OH) ₄ /Al ₂ O ₃ ·2SiO ₂ ·2H ₂ O	3.8
B5	Quartz	SiO ₂	29.9
	Albite	NaAlSi ₃ O ₈	70.1
B6	Quartz	SiO ₂	3.1
	Gypsum	CaSO ₄ ·2H ₂ O	77.0
	Kaolinite	Al ₂ Si ₂ O ₅ (OH) ₄ /Al ₂ O ₃ ·2SiO ₂ ·2H ₂ O	19.2
	Anatase	TiO ₂	0.6
B7	Quartz	SiO ₂	75.3
	Gypsum	CaSO ₄ ·2H ₂ O	4.5
	Illite	KAl ₂ Si ₃ AlO ₁₀ (OH) ₂	12.8
	Kaolinite	Al ₂ Si ₂ O ₅ (OH) ₄ /Al ₂ O ₃ ·2SiO ₂ ·2H ₂ O	5.9
	Anhydrite	CaSO ₄	1.5
B8	Quartz	SiO ₂	47.3
	Gypsum	CaSO ₄ ·2H ₂ O	21.3
	Kaolinite	Al ₂ Si ₂ O ₅ (OH) ₄ /Al ₂ O ₃ ·2SiO ₂ ·2H ₂ O	2
	Calcite	CaCO ₃	3.2
	Albite	NaAlSi ₃ O ₈	4.6
	Minamite	(Na,Ca) _{1-x} Al ₃ (SO ₄) ₂ (OH) ₆	2.4
	Halite	NaCl	0.8
B9	Quartz	SiO ₂	31.3
	Gypsum	CaSO ₄ ·2H ₂ O	49.2
	Kaolinite	Al ₂ Si ₂ O ₅ (OH) ₄ /Al ₂ O ₃ ·2SiO ₂ ·2H ₂ O	6.4
	Illite	KAl ₂ Si ₃ AlO ₁₀ (OH) ₂	4.1
	Albite	NaAlSi ₃ O ₈	8.9

6. Mineral Potential Map

The final potential location of mineralization was created by combining multi-criteria data. This allows for revealing the prospective areas of hydrothermal mineralization associated with hydrothermal alteration zones; thus, we use a variety of ways to emphasize alteration zones. The results of remote sensing analysis data were integrated using GIS approaches (band ratio, PC, mineral indices). These images were quantified and divided into various zones (different probability values). To obtain the prospective or promising map of mineral exploration, a succession of evidential maps is used. The approach of merging data in a GIS enabled the promotion and identification of the best exploration and mining locations. This aided exploration and the prediction of new mineralized zones. The recent innovative procedures that use recent digital technologies and creative geo-information approaches have allowed for the detection of the optimal mineral resource area. Multiple datasets have been aggregated and integrated since the birth of the GIS to locate new mineralized zones [63] reliably.

Using a GIS-based overlay method, the likely locations of hydrothermal mineral deposits were revealed by combining several evidence hydrothermal alteration maps (Figure 9). The mineral prospective map is divided into six groups (Figure 9a) based on their prospective for hydrothermal alteration amplitude: very low, low, moderate, good, very good, and excellent, and covers 31.36, 28.22, 20.49, 10.99, 6.35, and 2.59 % percent of the research region, respectively. The red color indicates the most promising mineral deposit zone. The resulting map (Figure 9) demonstrates a pattern of coherence in the

hydrothermal-ore deposits found in the area's mines. Many sections of the potentially high zone, meanwhile, were restricted to wadi deposits and areas of sedimentary cover in the northeast of the research area.

7. Discussion

The use of various methodologies for three different sensors, including OLI, Sentinel-2, and ASTER data, clearly shows that hydrothermal alteration processes dominate the examined area. This is because identifying HAZs through fracture/fault zones is required when exploring mineral deposits that originated from hydrothermal processes [2,5,8]. As a result, the severity of the alteration can help determine where the ore body is located.

The areas of HAZs (Figure 4) were identified using band ratios generated from OLI sensors such as $6/7$, $6/2$, and $6/5 * 4/5$ [16], $6/7$, $6/5$, 5 [56], and $6/7$, $4/2$, $5/6$ [7]. Because hydrothermal activities alter the physical and chemical characteristics of country rocks, they change. Band ratio $6/7$ emphasized OH-bearing minerals such as kaolinite–smectite, micas, and amphiboles [23]. Iron-bearing minerals, on the other hand, are delineated utilizing band ratios such as $4/2$, $6/5$, and $6/5 * 4/5$ [16,17]. Furthermore, applying Sentinel-2 band ratio $3/4$ characterizes the ferrous iron, the ferric oxides (Fe^{3+}) represented by $11/8A$, and ferrous iron (Fe^{2+}) represented by $(3/4)$ [55]. In addition to Sentinel-2 band ratios, $11/12$ marks the OH-bearing minerals [2]. This is because the integration of iron-bearing minerals mixed with OH-bearing minerals from different sensors (OLI and Sentinel-2) characterized the gossans and iron-rich zones [28,64], as displayed in Figures 3 and 4.

Following that, the SWIR ASTER data was analyzed using various band ratios to look for areas of hydrothermal alteration, comprising $4/6$, $4/5$, and $4/7$; $4/6$, $7/6$, and $(5 + 7)/6$; $(5 + 7)/6$, PC2, MNF3; OHI, KAI, and ALI, and PC2 of PCA OHI, KAI, and ALI and Calcite. Delineation of OH-bearing minerals was possible because of the use of a band ratio of $4/6$ ($\lambda = 1.656/2.209$ m) (Figure 7). The $4/6$ ratio is excellent for accentuating hydrous minerals like kaolinite, illite, and montmorillonite because they have a high absorption signature in band 6 and a high reflectance in band 4. Furthermore, ASTER band ratios $4/5$ and $4/7$ boost argillic and sericitic alteration zones, respectively [2,6]. The white tone in Figures 7 and 8 highlights areas of hydrothermal alteration, which for the most part, aligns with structural connections.

The relative band depth $(5 + 7)/6$ was efficiently adopted (Figures 7c and 8a) for excellent detection of Al–smectite, muscovite, sericite, and illite [2,62,65], and Al/Fe-OH minerals, such as muscovite, kaolinite, and jarosite [66]. Moreover, ASTER bands $5 + 7/6$ 'Al-OH content' vs. bands $5/7$ (outside absorption) 'Al-OH composition' [62]. This diagram (Figure 8c) shows that the selected red pixels are rich in AL-OH, but the lowest ones are in green. The AL-OH area rich in minerals that are marked in red is consistent with the areas of high hydrothermal alteration.

Using GIS-based weighted overlay analysis to confirm the findings of band ratios and mineral indices acquired from Landsat-OLI, Sentinel-2, and ASTER data that revealed iron-containing and Al-OH-carrying minerals revealed useful information regarding places rich in gossans. Such gossans that consist of limonite, goethite, hematite, malachite, and azurite reveal the existence of massive sulfide; porphyry and skarn deposits [64] are consistent with areas of high hydrothermal alteration intensity.

8. Conclusions

The Khnaiguiyah area, Saudi Arabia, is tested to delineate the area of probable mineral resources. The ability of multispectral remote sensing data to detect and characterize the hydrothermal alteration minerals is significant for mineral exploration. The present study used ASTER, Sentinel-2, and Landsat-OLI to identify potential areas of HAZs. The HAZs generated from these various multispectral sensors were combined through GIS to highlight the potential areas of HAZs. The highest grade of HAZs, which covers about 2.59 %, is compatible with areas of significant hydrothermal changes and has been verified with areas of gossans that revealed the presence of sulfide minerals.

Author Contributions: Conceptualization, M.A. (Mohamed Abdelkareem); methodology, M.A. (Mohamed Abdelkareem) and S.S.A.; software, I.S.A.; validation, M.A. (Mohamed Abdelkareem), S.S.A., and F.A.; investigation, M.A. (Mohamed Abdelkareem); resources, S.S.A.; writing—original draft preparation, M.A. (Mohamed Abdelkareem), F.A., A.M.A.-S., I.S.A., H.G. and M.A. (Mislal Alotaibi); writing—review and editing, M.A. (Mohamed Abdelkareem); visualization, M.A. (Mohamed Abdelkareem); funding acquisition, S.S.A. All authors have read and agreed to the published version of the manuscript.

Funding: This research was funded by King Saud University, grant number RSP2022R496. The APC was funded by King Saud University.

Acknowledgments: This research was supported by Researchers Supporting Project number (RSP2022R496), King Saud University, Riyadh, Saudi Arabia.

Conflicts of Interest: The authors declare no conflict of interest.

References

1. Shi, K.; Chang, Z.; Chen, Z.; Wu, J.; Yu, B. Identifying and evaluating poverty using multisource remote sensing and point of interest (POI) data: A case study of Chongqing, China. *J. Clean. Prod.* **2020**, *255*, 120245. [[CrossRef](#)]
2. Abdelkareem, M.; Al-Arifi, N. Synergy of Remote Sensing Data for Exploring Hydrothermal Mineral Resources Using GIS-Based Fuzzy Logic Approach. *Remote Sens.* **2021**, *13*, 4492. [[CrossRef](#)]
3. Mars, J.C.; Rowan, L.C. Regional mapping of phyllic- and argillic-altered rocks in the Zagros magmatic arc, Iran, using Advanced Spaceborne Thermal Emission and Reflection Radiometer (ASTER) data and logical operator algorithms. *Geosphere* **2006**, *2*, 161–186. [[CrossRef](#)]
4. Abdelkareem, M.; El-Baz, F. Characterizing hydrothermal alteration zones in Hamama area in the central Eastern Desert of Egypt by remotely sensed data. *Geocarto Int.* **2018**, *33*, 1307–1325. [[CrossRef](#)]
5. Crosta, A.P.; De Souza Filho, C.R.; Azevedo, F.; Brodie, C. Targeting key alteration minerals in epithermal deposits in Patagonia, Argentina, using ASTER imagery and principal component analysis. *Int. J. Remote Sens.* **2003**, *24*, 4233–4240. [[CrossRef](#)]
6. Testa, F.J.; Villanueva, C.; Cooke, D.R.; Zhang, L. Lithological and Hydrothermal Alteration Mapping of Epithermal, Porphyry and Tourmaline Breccia Districts in the Argentine Andes Using ASTER Imagery. *Remote. Sens.* **2018**, *10*, 203. [[CrossRef](#)]
7. Abrams, M.J.; Brown, D.; Lepley, L.; Sadowski, R. Remote sensing for porphyry copper deposits in southern Arizona. *Econ. Geol.* **1983**, *78*, 591–604. [[CrossRef](#)]
8. Sabins, F. *Remote Sensing Principles and Interpretation*, 3rd ed.; W.H. Freeman Company: New York, NY, USA, 1997; p. 494.
9. Sabins, F.F. Remote sensing for mineral exploration. *Ore Geol. Rev.* **1999**, *14*, 157–183. [[CrossRef](#)]
10. Shi, X.; Al-Arifi, N.; Abdelkareem, M.; Abdalla, F. Application of remote sensing and GIS techniques for exploring potential areas of hydrothermal mineralization in the central Eastern Desert of Egypt. *J. Taibah Univ. Sci.* **2020**, *14*, 1421–1432. [[CrossRef](#)]
11. Ninomiya, Y. A stabilized vegetation index and several mineralogic indices defined for ASTER VNIR and SWIR data. In Proceedings of the 2003 IEEE International Geoscience and Remote Sensing Symposium, Toulouse, France, 21–25 July 2003; pp. 1552–1554.
12. Ninomiya, Y. Advanced remote lithologic mapping in ophiolite zone with ASTER multispectral thermal infrared data. In Proceedings of the 2003 IEEE International Geoscience and Remote Sensing Symposium, Toulouse, France, 21–25 July 2003; pp. 1561–1563.
13. Rowan, L.C.; Mars, J.C. Lithologic mapping in the Mountain Pass, California area using advanced spaceborne thermal emission and reflection radiometer (ASTER) data. *Remote Sens. Environ.* **2003**, *84*, 350–366. [[CrossRef](#)]
14. Azizi, H.; Tarverdi, M.; Akbarpour, A. Extraction of hydrothermal alterations from ASTER SWIR data from east Zanjan, northern Iran. *Adv. Space Res.* **2010**, *46*, 99–109. [[CrossRef](#)]
15. Zhang, X.; Pazner, M.; Duke, N. Lithologic and mineral information extraction for gold exploration using ASTER data in the south Chocolate Mountains (California). *ISPRS J. Photogramm. Remote. Sens.* **2007**, *62*, 271–282. [[CrossRef](#)]
16. Sultan, M.; Arvidson, R.E.; Sturchio, N.C. Mapping of serpentinites in the Eastern Desert of Egypt by using Landsat thematic mapper data. *Geology* **1986**, *14*, 995–999. [[CrossRef](#)]
17. Madani, A.M. Utilization of Landsat ETM+ Data for Mapping Gossans and Iron Rich Zones Exposed at Bahrah Area, Western Arabian Shield, Saudi Arabia. *J. King Abdulaziz Univ. Sci.* **2009**, *20*, 35–49. [[CrossRef](#)]
18. Ramadan, T.M.; Kontry, A. Mineralogical and structural characterization of alteration zones detected by orbital remote sensing at Shalatein District, SE Desert, Egypt. *J. Afr. Earth Sci.* **2004**, *40*, 89–99. [[CrossRef](#)]
19. Cardoso-Fernandes, J.; Teodoro, A.C.; Lima, A.; Perrotta, M.; Roda-Robles, E. Detecting Lithium (Li) Mineralizations from Space: Current Research and Future Perspectives. *Appl. Sci.* **2020**, *10*, 1785. [[CrossRef](#)]
20. El-Din, G.M.K.; El-Noby, M.E.; Abdelkareem, Z.M.; Hamimi, Z. Using multispectral and radar remote sensing data for geological investigation, Qena-Safaga Shear Zone, Eastern Desert, Egypt. *Arab. J. Geosci.* **2021**, *14*, 997. [[CrossRef](#)]
21. Galvão, L.S.; Almeida-Filho, R.; Vitorello, I. Spectral discrimination of hydrothermally altered materials using ASTER short-wave infrared bands: Evaluation in a tropical savannah environment. *Int. J. Appl. Earth Obs. Geoinf.* **2005**, *7*, 107–114. [[CrossRef](#)]

22. Yamaguchi, Y.; Naito, C. Spectral indices for lithologic discrimination and mapping by using the ASTER SWIR bands. *Int. J. Remote Sens.* **2003**, *24*, 4311–4323. [[CrossRef](#)]
23. Gupta, R.P. *Remote Sensing Geology*, 2nd ed.; Springer-Verlag: Berlin/Heidelberg, Germany, 2003.
24. Crowley, J.K.; Brickey, D.W.; Rowan, L.C. Airborne imaging spectrometer data of the Ruby Mountains, Montana: Mineral discrimination using relative absorption band-depth images. *Remote Sens. Environ.* **1989**, *29*, 121–134. [[CrossRef](#)]
25. Zhang, N.; Zhou, K. Mineral prospectivity mapping with weights of evidence and fuzzy logic methods. *J. Intell. Fuzzy Syst.* **2015**, *29*, 2639–2651. [[CrossRef](#)]
26. Harris, J.R.; Wilkinson, L.; Heather, K.; Fumerton, S.; Bernier, M.A.; Ayer, J.; Dahn, R. Application of GIS Processing Techniques for Producing Mineral Prospectivity Maps—A Case Study: Mesothermal Au in the Swayze Greenstone Belt, Ontario, Canada. *Nonrenewable Resour.* **2001**, *10*, 91–124. [[CrossRef](#)]
27. Abdelkareem, M.; Othman, I.; Kamal El Din, G. Lithologic mapping using remote sensing data in Abu Marawat Area, Eastern Desert of Egypt. *Int. J. Adv. Remote Sens. GIS.* **2017**, *6*, 2171–2177. [[CrossRef](#)]
28. Abdelkareem, M.K.; El-Din, G.; Osman, I. An integrated approach for mapping mineral resources in the Eastern Desert of Egypt. *Int. J. Appl. Earth Obs. Geoinf.* **2018**, *73*, 682–696. [[CrossRef](#)]
29. Sun, T.; Chen, F.; Zhong, L.; Liu, W.; Wang, Y. GIS-based mineral prospectivity mapping using machine learning methods: A case study from Tongling ore district, eastern China. *Ore Geol. Rev.* **2019**, *109*, 26–49. [[CrossRef](#)]
30. Campos, L.D.; de Souza, S.M.; de Sordi, D.A.; Tavares, F.M.; Klein, E.L.; Lopes, E.C.D.S. Predictive mapping of prospectivity in the Gurupi orogenic gold belt, north–northeast Brazil: An example of districts scale mineral system approach to exploration targeting. *Nat. Resour. Res.* **2017**, *26*, 509–534. [[CrossRef](#)]
31. Stern, R.J.; Johnson, P.R.; Kröner, A.; Yibas, B. Neoproterozoic ophiolites of the Arabian-Nubian shield. *Dev. Precambrian Geol.* **2004**, *13*, 95–128.
32. Kröner, A.; Stern, R.J. Pan-African Orogeny. *Encycl. Geol.* **2004**, *1*, 1–12.
33. Stoeser, D.B.; Camp, V.E. Pan-African microplate accretion of the Arabian Shield. *Geol. Soc. Am. Bull.* **1985**, *96*, 817–826. [[CrossRef](#)]
34. Johnson, P.R.; Woldehaimanot, B. *Development of the Arabian-Nubian Shield: Perspectives on Accretion and Deformation in the Northern East African Orogen and the Assembly of Gondwana*; Geological Society, London, Special Publications: London, UK, 2003; Volume 206, pp. 289–325.
35. Genna, A.; Nehlig, P.; Le Goff, E.; Guerrot, C.; Shanti, M. Proterozoic tectonism of the Arabian Shield. *Precambrian Res.* **2002**, *117*, 21–40. [[CrossRef](#)]
36. Nehlig, P.; Genna, A.; Asfirane, F.; BRGM France; Guerrot, C.; Eberlé, J.; Kluyver, H.; Lasserre, J.; Le Goff, E.; Nicol, N.; et al. A review of the Pan-African evolution of the Arabian Shield. *GeoArabia* **2002**, *7*, 103–124. [[CrossRef](#)]
37. Hamimi, Z.; Fowler, A.R. Najd Shear System in the Arabian-Nubian Shield. In *The Geology of the Arabian-Nubian Shield*; Springer: Cham, Switzerland, 2021; pp. 359–392.
38. Hamimi, Z.; Abdelkareem, M.; Fowler, A.R.; Younis, M.H.; Matsah, M.; Abdalla, F. Remote sensing and structural studies of the Central Asir Shear Zone, Western Arabian Shield: Implications for the late Neoproterozoic EW Gondwana assembly. *J. Asian Earth Sci.* **2021**, *215*, 104782. [[CrossRef](#)]
39. Johnson, P.R.; Andresen, A.; Collins, A.S.; Fowler, A.R.; Fritz, H.; Ghebreab, W.; Kusky, T.; Stern, R.J. Late Cryogenian–Ediacaran history of the Arabian–Nubian Shield: A review of depositional, plutonic, structural, and tectonic events in the closing stages of the northern East African Orogen. *J. Afr. Earth Sci.* **2011**, *61*, 167–232. [[CrossRef](#)]
40. Doebrich, J.L.; Al-Jehani, A.M.; Siddiqui, A.A.; Hayes, T.S.; Wooden, J.L.; Johnson, P.R. Geology and metallogeny of the Ar Rayn terrane, eastern Arabian shield: Evolution of a Neoproterozoic continental-margin arc during assembly of Gondwana within the East African orogen. *Precambrian Res.* **2007**, *158*, 17–50. [[CrossRef](#)]
41. BRGM Geoscientists. *Khnaiguiyah Zinc-Copper Deposit Prefeasibility Study: Saudi Arabian Directorate General of Mineral Resources*; Technical Report BRGM-TR-13-4; French Geological Survey: Orléans, France, 1994.
42. Vaslet, D.; Delfour, J.; Manivit, J.; Le Nindre, Y.M.; Brosse, J.M.; Fourniquet, J. *Geologic Map of the Wadi ar Rayn Quadrangle, Sheet 23H, Kingdom of Saudi Arabia*; Saudi Arabian Deputy Ministry for Mineral Resources: Jeddah, Saudi Arabia, 1983.
43. Mahdevar, M.R.; Ketabi, P.; Saadatkhah, N.; Rahnamarad, J.; Mohammadi, S.S. Application of ASTER SWIR data on detection of alteration zone in the Sheikhabad area, eastern Iran. *Arab. J. Geosci.* **2015**, *8*, 5909–5919. [[CrossRef](#)]
44. Hosseinjani Zadeh, M.; Tangestani, M.H.; Roldan, F.V.; Yusta, I. Mineral exploration and alteration mapping using mixture tuned matched filtering approach on ASTER data at the central part of Dehaj-Sarduiyeh copper belt, SE Iran. *IEEE J. Sel. Topics Appl. Earth Obs. Remote Sens.* **2014**, *7*, 284–289. [[CrossRef](#)]
45. Rowan, L.C.; Goetz, A.F.H.; Ashley, R.P. Discrimination of Hydrothermally Altered and Unaltered Rocks in Visible and Near Infrared Multispectral Images. *Geophysics* **1977**, *42*, 522–535. [[CrossRef](#)]
46. Mather, P.M.; Koch, M. *Computer Processing of Remotely-Sensed Images: An Introduction*; John Wiley & Sons: Hoboken, NJ, USA, 2011.
47. Goetz, A.F.H.; Rock, B.N.; Rowan, L.C. Remote sensing for exploration; an overview. *Econ. Geol.* **1983**, *78*, 573–590. [[CrossRef](#)]
48. Inzana, J.; Kusky, T.; Tucker, R. Comparison of TM Band Ratio Images, Supervised Classifications, and Merged TM and Radar Imagery for Structural Geology Interpretations of the Central Madagascar Highlands. In Proceedings of the American Society of Photogrammetry and Remote Sensing, Annual Meeting, Abstracts with Programs, London, UK, 12–14 September 2001; p. 34.

49. Kusky, T.; Ramadan, T.M. Structural controls on Neoproterozoic mineralization in the South Eastern Desert, Egypt: An integrated field, Landsat TM, and SIR-C/X SAR approach. *J. Afr. Earth Sci.* **2002**, *35*, 107–121. [[CrossRef](#)]
50. Volesky, J.C.; Stern, R.J.; Johnson, P.R. Geological control of massive sulfide mineralization in the Neoproterozoic Wadi Bidah shear zone, southwestern Saudi Arabia, inferences from orbital remote sensing and field studies. *Precambrian Res.* **2003**, *123*, 235–247. [[CrossRef](#)]
51. Gad, S.; Kusky, T. Lithological mapping in the Eastern Desert of Egypt, the Barramiya area, using Landsat thematic mapper (TM). *J. Afr. Earth Sci.* **2006**, *44*, 196–202. [[CrossRef](#)]
52. Boardman, W.; Kruse, F.A. *Automated Spectra Analysis: A Geologic Example Using AVIRIS Data, North Grapevine on Geologic Remote Sensing*; Environmental Research Institute of Michigan: Ann Arbor, MI, USA, 1994; pp. 407–418.
53. Joly, A.; Porwal, A.; McCuaig, T.C.; Chudasama, B.; Dentith, M.C.; Aitken, A.R.A. Mineral systems approach applied to GIS-based 2D-prospectivity modelling of geological regions: Insights from Western Australia. *Ore Geol. Rev.* **2015**, *71*, 673–702. [[CrossRef](#)]
54. Carranza, E.; Hale, M.; Faassen, C. Selection of coherent deposit-type locations and their application in data-driven mineral prospectivity mapping. *Ore Geol. Rev.* **2008**, *33*, 536–558. [[CrossRef](#)]
55. Carranza, E.J.M.; Laborte, A.G. Data-driven predictive mapping of gold prospectivity, Baguio district, Philippines: Application of random forests algorithm. *Ore Geol. Rev.* **2015**, *71*, 777–787. [[CrossRef](#)]
56. Ge, W.; Cheng, Q.; Jing, L.; Wang, F.; Zhao, M.; Ding, H. Assessment of the Capability of Sentinel-2 Imagery for Iron-Bearing Minerals Mapping: A Case Study in the Cuprite Area, Nevada. *Remote. Sens.* **2020**, *12*, 3028. [[CrossRef](#)]
57. Ramadan, E.; Feng, X.-Z.; Cheng, Z. Satellite remote sensing for urban growth assessment in Shaoxing City, Zhejiang Province. *J. Zhejiang Univ. A* **2004**, *5*, 1095–1101. [[CrossRef](#)] [[PubMed](#)]
58. Ahmed, A.; Abdelkareem, M.; Asran, A.M.; Mahran, T.M. Geomorphic and lithologic characteristics of Wadi Feiran basin, southern Sinai, Egypt, using remote sensing and field investigations. *J. Earth Syst. Sci.* **2017**, *126*, 1–25. [[CrossRef](#)]
59. El-Din, G.K.; Abdelkareem, M. Integration of remote sensing, geochemical and field data in the Qena-Safaga shear zone: Implications for structural evolution of the Eastern Desert, Egypt. *J. Afr. Earth Sci.* **2018**, *141*, 179–193. [[CrossRef](#)]
60. Olmo, M.C.; Abarca, F.; Rigol, J.P.; Rigol-Sanchez, J.P. Development of a Decision Support System based on remote sensing and GIS techniques for gold-rich area identification in SE Spain. *Int. J. Remote Sens.* **2002**, *23*, 4801–4814. [[CrossRef](#)]
61. Brandmeier, M. Remote sensing of Carhuarazo volcanic complex using ASTER imagery in Southern Peru to detect alteration zones and volcanic structures—A combined approach of image processing in ENVI and ArcGIS/ArcScene. *Geocarto Int.* **2010**, *25*, 629–648. [[CrossRef](#)]
62. Bolouki, S.M.; Ramazi, H.R.; Maghsoudi, A.; Pour, A.; Sohrabi, G. A Remote Sensing-Based Application of Bayesian Networks for Epithermal Gold Potential Mapping in Ahar-Arasbaran Area, NW Iran. *Remote Sens.* **2020**, *12*, 105. [[CrossRef](#)]
63. Cudahy, T.J.; Jones, M.; Thomas, M.; Laukamp, C.; Caccetta, M.; Hewson, R.D.; Rodger, A.D.; Verrall, M. *Next Generation Mineral Mapping: Queensland Airborne HyMap and Satellite ASTER Surveys, 2006–2008*; CSIRO Exploration and Mining: Canberra, Australia, 2008.
64. Zeghouane, H.; Allek, K.; Kesraoui, M. GIS-based weights of evidence modeling applied to mineral prospectivity mapping of Sn-W and rare metals in Laouni area, Central Hoggar, Algeria. *Arab. J. Geosci.* **2016**, *9*, 373. [[CrossRef](#)]
65. Gahlan, H.; Ghrefat, H. Detection of Gossan Zones in Arid Regions Using Landsat 8 OLI Data: Implication for Mineral Exploration in the Eastern Arabian Shield, Saudi Arabia. *Nat. Resour. Res.* **2018**, *27*, 109–124. [[CrossRef](#)]
66. Sekandari, M.; Masoumi, I.; Pour, A.B.; Muslim, A.M.; Rahmani, O.; Hashim, M.; Zoheir, B.; Pradhan, B.; Misra, A.; Aminpour, S.M. Application of Landsat-8, Sentinel-2, ASTER and WorldView-3 Spectral Imagery for Exploration of Carbonate-Hosted Pb-Zn Deposits in the Central Iranian Terrane (CIT). *Remote Sens.* **2020**, *12*, 1239. [[CrossRef](#)]